PERGAMON

Acta mater. 48 (2000) 2815–2822

Acta MATERIALIA

www.elsevier.com/locate/actamat

THE USE OF TERNARY PHASE DIAGRAMS IN THE STUDY OF HIGH TEMPERATURE CORROSION PRODUCTS FORMED ON Fe–5 WT% Al ALLOYS IN REDUCING AND OXIDIZING ENVIRONMENTS

S. W. BANOVIC†, J. N. DUPONT and A. R. MARDER

Department of Materials Science and Engineering, Lehigh University, Bethlehem, PA 18015, USA

(Received 18 February 2000; accepted 28 March 2000)

Abstract—Ternary phase diagrams, in conjunction with microscopy techniques and reaction product chemistries, were used to describe the possible "diffusion paths" and resulting morphologies that may occur during formation of corrosion scales from high temperature gaseous exposure. Iron with 5 wt% of aluminum was exposed to reducing and oxidizing environments at 700°C. Characterization of the surface reaction products was conducted using microscopy techniques with energy dispersive spectroscopy and electron probe microanalysis. Under both conditions, iron diffused outward to form surface reaction products, either iron sulfide or iron oxide. The ingress of sulfur or oxygen through the previously formed reaction products was found to produce internal corrosion phases within the alloy. By plotting chemical information acquired from the corrosion scales on ternary phase diagrams, development of the phase layer sequence and morphologies of the multiphase corrosion scales was schematically explained. This analysis was conducted using conventions summarized by Clarke (*Trans. Am. Inst. Min. Engrs*, 1963, **227**, 1250) for plotting diffusion paths in multiphase ternary diffusion studies from solid-state reactions. By presenting the experimental data in this manner, the morphological development of the scales was related to the composition path on the ternary phase diagrams.

Keywords: Fe–Al alloys; High temperature; Gaseous; Corrosion; Phase diagrams

1. INTRODUCTION

High temperature gaseous corrosion is a problem encountered in fossil-fired boilers operating in the utility industry. High wastage rates of the boiler tube walls can occur by means of corrosion reactions between the corrosive by-products produced by burning coal and the tube material (typically a low alloy steel) that form non-protective surface scales. Therefore, many new corrosion resistant compositions are being identified and evaluated, with the corrosion behavior of the alloy as a critical factor in determining its use for industrial application. Presently, iron–aluminum alloys, in the form of weld overlay coatings, are one of these candidates. These materials have shown excellent corrosion resistance to both oxidizing [1–5] and sulfidizing [6–21] environments. However, a detailed description of their scale development has not been conducted.

It has been observed that an important factor controlling the overall corrosion rate of a material is the type and morphology of the reaction surface product that forms on an alloy during exposure [22, 23]. Hence, characterization of these corrosion scales is crucial in understanding the protective/non-protective nature of the phase(s) that may develop. This is usually conducted through alloy exposure to the corrosive gas of interest at temperature followed by post-exposure analysis of the corrosion products. Typical analysis for the scales include microscopy (light optical and electron), chemical analysis (e.g. energy dispersive spectroscopy, electron probe microanalysis, Auger spectroscopy, secondary ion microscopy), and crystal structure determination (e.g. X-ray diffraction). These techniques provide an understanding of the corrosion reactions taking place, but do not shed any light on the phase layer sequence or morphological developments. Other types of corrosion analyses [24], such as solid–solid diffusion couple studies between the scale material and alloy, have been conducted which investigated the phase layer sequence, morphology, and phase equilibria of the

† To whom all correspondence should be addressed.

1359-6454/00/$20.00
PII: S1359-6454(00)00095-1

corrosion reactions. This was examined through application of solid-state diffusion couple techniques, microscopy, and plotting of chemical composition profiles using diffusion path conventions described by Clark [25]. The analysis entailed both the physical aspects of the corrosion products as well as described their morphological development. As gaseous corrosion studies proceed from gas–solid reactions at the alloy–scale interface upon initial exposure to solid–solid diffusion couples between the alloy and reaction scale formed at extended times, a similar type of analysis was conducted for samples exposed to high temperature gaseous exposure. These studies were performed on iron–aluminum alloys in both oxidizing and sulfidizing environments.

2. EXPERIMENTAL PROCEDURE

The Fe–Al alloys used during this research were produced at Oak Ridge National Laboratory (Oak Ridge, TN) by arc melting high purity Fe (99.99%) and Al (99.99%) under argon and drop casting into a water cooled copper mold. Substrates, with dimensions of 1 cm × 1 cm × 2 mm, were sectioned from the bulk using a high speed diamond saw followed by grinding of the surface to 600 grit. Specimens were prepared immediately before insertion into the balance with prior steps of ultrasonic cleaning in soapy water and methanol. A Netzsch STA 409 high temperature thermogravimetric balance was used to maintain stringent control on the testing parameters, i.e. temperature, gas composition, and exposure time. The samples were isothermally held at 700°C for 50 h in two gas types. For the reducing atmosphere, an argon base gas containing 0.1% H_2–1.0% H_2S–5 p.p.m. O_2 (by volume) was used to maintain a partial pressure of sulfur [$p(S_2)$] and oxygen [$p(O_2)$] at 10^{-4} and 10^{-25} atm, respectively, at temperature. The $p(O_2)$ was determined using a solid state oxygen detector and the $p(S_2)$ was calculated using the SolGasMix program [26]. The oxidizing atmosphere was produced by flowing zero grade air into the chamber.

Corroded samples were mounted in cold setting epoxy with subsequent grinding procedures to 1200 grit with silicon carbide papers. A final polishing step was conducted using 1.0 μm diamond paste on a low nap cloth. Further polishing with any type of colloidal alumina or silica was avoided in order to minimize any possibilities of contamination or pullout of the scale. The use of 200 proof, dehydrated ethanol was used for both lubrication and cleansing solutions during preparation of samples from the reducing environment in order to avoid degradation of the corrosion products from water [27]. Post-exposure characterization of the polished cross-sections was conducted using light optical and scanning electron microscopy. For the latter, a JEOL 6300F scanning electron microscope, with an Oxford (Link) energy dispersive spectroscopy (EDS) system capable of detecting light elements, was employed. Quantitative chemical information was obtained using a JEOL 733 electron probe micro analyzer (EPMA) equipped with wavelength dispersive spectrometers (WDS). The accelerating voltage and probe current were 20 kV and 50 nA, respectively. K_α X-ray lines were analyzed and counts con-

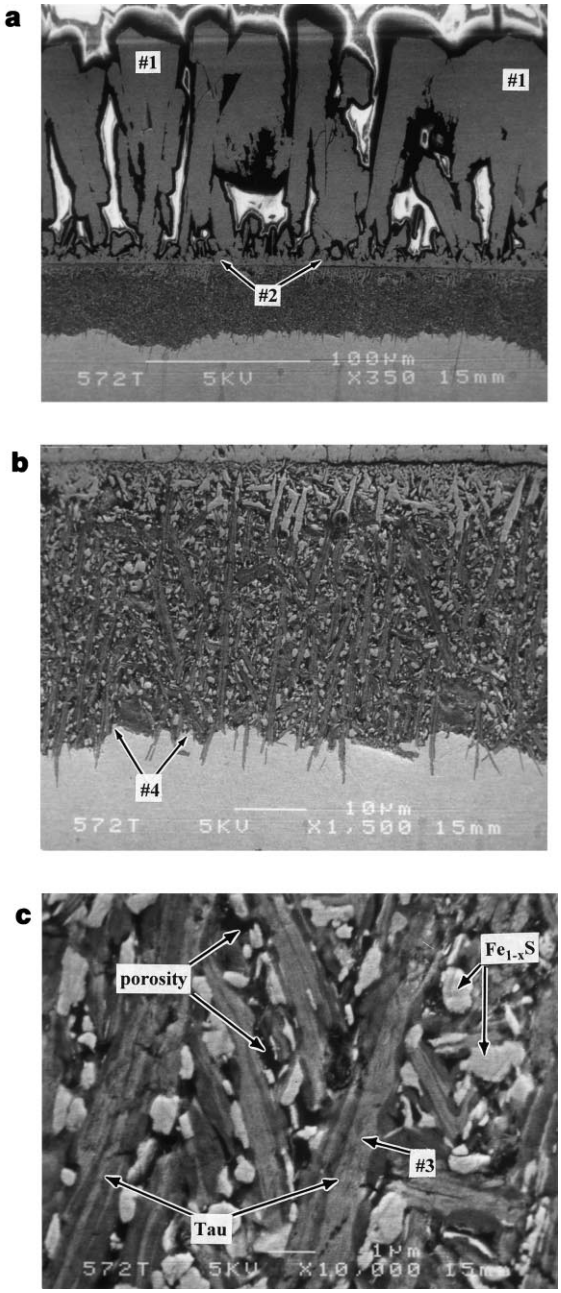

Fig. 1. Cross-sectional secondary electron micrographs of the corrosion scale formed on the Fe–5 wt% Al alloy in the sulfidizing atmosphere after 50 h of exposure. The points display the location of EPMA analysis as displayed in Table 1: (a) full scale; (b) inner layer; (c) higher magnification of the inner scale.

Table 1. EPMA data, in wt%, obtained for the corrosion scale formed in the reducing environment on the Fe–Al alloy. Points correspond to Fig. 1

Point	Scale feature	Fe	Al	S	Phase(s)
1	Outer columnar scale	61.7 ± 0.5	0.0	37.7 ± 0.3	$Fe_{1-x}S$
2	Base of outer scale	61.7 ± 0.5	0.9 ± 0.2	37.6 ± 0.4	$Fe_{1-x}S$ with Al
	Scan of inner layer	45.1 ± 0.3	8.3 ± 0.5	43.3 ± 0.7	$\tau + Fe_{1-x}S$
3	Dark, inner layer plate	24.0 ± 0.8	20.7 ± 0.3	52.8 ± 1.0	τ
4	Substrate near scale	95.4 ± 0.3	4.9 ± 0.1	0.0	α-(Fe)
	Alloy at far distances	95.7 ± 0.3	4.9 ± 0.5	0.0	α-(Fe)

verted to weight percentages using a $\varphi(\rho z)$ correction scheme [28].

3. RESULTS

3.1. Reducing environment morphologies

Examination of the Fe–5Al samples after exposure in the reducing environment revealed the development of a bilayered, thick surface scale, Fig. 1. The compositional data for these phases can be found in Table 1. The outer scale was composed of irregularly shaped plates that had the appearance of being somewhat columnar in cross-section. EPMA data, point **1**, indicated that they were iron sulfide ($Fe_{1-x}S$), with minor quantities of aluminum, approximately 1 wt%, dissolved in solution at their base (point **2**). A secondary electron micrograph of the inner scale revealed that it was a porous, two-phase region of dark gray plates and light gray particles with some porosity, Figs 1(b) and (c). Quantitative chemical information of the inner layer as a whole was obtained by sampling areas, approximately 25 μm^2, of this region. As described below, the results placed it in a two-phase region of tau (τ), a spinel-type compound ($FeAl_2S_4$), and iron sulfide. Point analysis (point **3**) of the dark gray plates indicated that they were τ, with some compositional variation. Quantitative compositions of the light gray particles could not be obtained using EPMA due to their size. However, from their coloring in LOM and qualitative EDS analysis of high Fe and S counts and low aluminum, they were assumed to be iron sulfide. Higher magnification of the τ-phase revealed light colored striations in some of the plates, Fig. 1(c). While these striations were too small to quantitatively analyze individually, it is believed that they may be present due to a decomposition process of the τ-phase that occurred upon cooling from high temperature exposure. Mrowec and co-workers [29, 30] surmised this type of decomposition during sulfidation experiments on FeCr alloys where a complex $Fe(Fe_xCr_{2-x})S_4$ spinel was believed to have decomposed into sulfides that were more stable at room temperature ($FeCr_2S_4$, FeS, and Cr_2S_3). Attack at the alloy–scale interface [bottom of Fig. 1(b)] showed the protrusion of the plates into the substrate. Again, quantitative chemical information could not be obtained from the tips due to their size, but EDS analysis showed high counts of aluminum, iron, and sulfur indicating the possible continuation of the τ-phase. Unaffected base metal near the protrusions, point **4**, showed no increase in the amount of sulfur or decrease in aluminum and iron when compared with the alloy at far distances.

3.2. Oxidation environment morphologies

For the 5 wt% Al sample in the oxidizing atmosphere, nodule formations of oxide product were observed on the surface, Fig. 2. This type of morphology occurred due to the simultaneous development of a thin, passive alumina (Al_2O_3) scale with coinciding growth of iron oxide products [31]. In cross-section, Fig. 3, the nodules were found to consist of multi-layered phases with varying compositions. EPMA data obtained for these phases can be found in Table 2. The outermost layer was compact with analysis indicating that it was Fe_2O_3 (hematite). The darker gray phase below this was magnetite, Fe_3O_4. Some porosity, possibly pullout due to the metallographic preparation of the samples, can be observed at the inner scale–outer scale interface, Fig. 3(b). While the corrosion product found protruding into the substrate appeared to be homogeneous, Fig. 3(c), its composition resided near the corner of a multiphase region (Fe_2O_3–Fe_3O_4–Al_2O_3) on the ternary diagram. Higher magnification of the next layer revealed in-

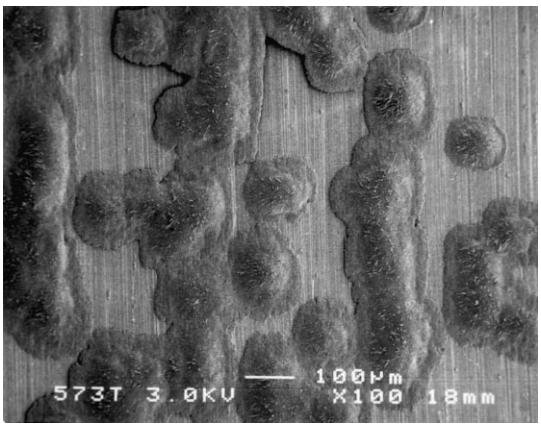

Fig. 2. Secondary electron micrograph showing the development of oxide nodules on the surface of the Fe–5 wt% Al alloy exposed to the oxidizing environment for 50 h.

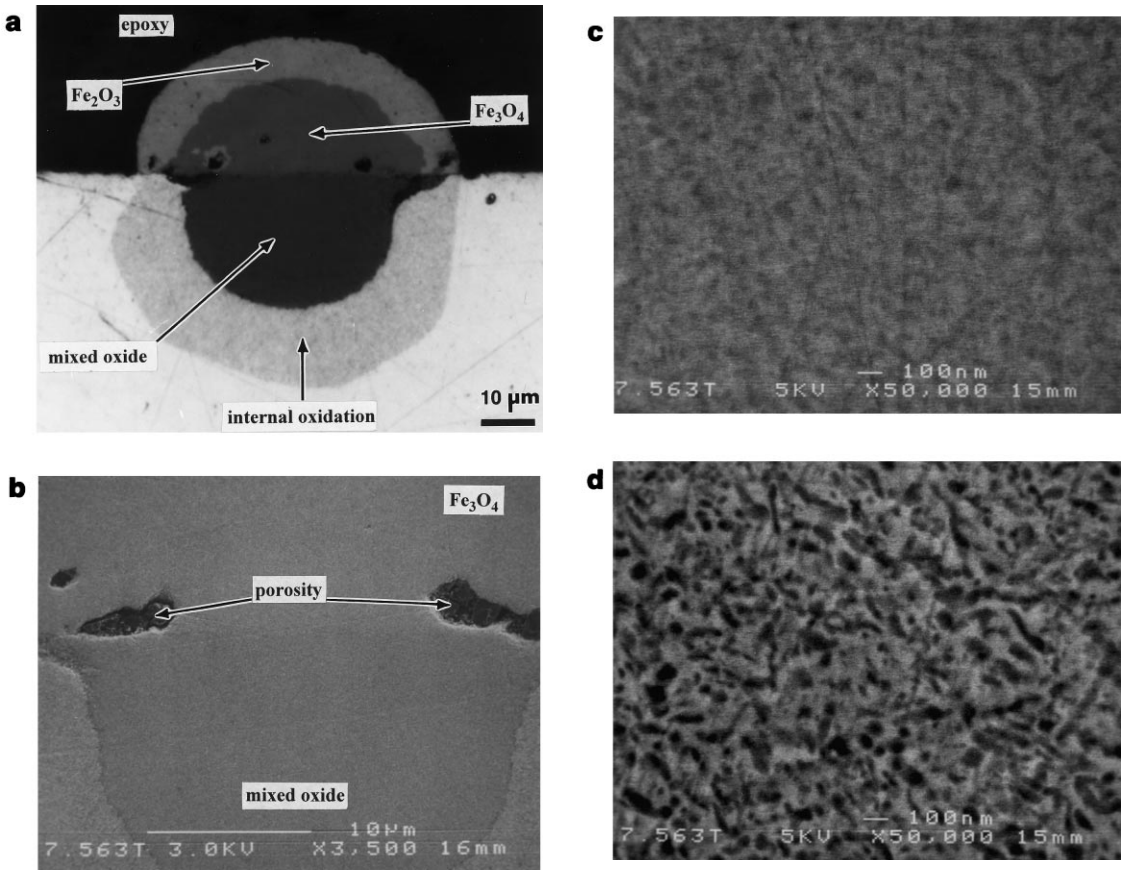

Fig. 3. Cross-sectional micrographs of the corrosion phases formed on the Fe–5 wt% Al alloy in the oxidizing environment after 50 h of exposure. EPMA analyses of the phases are given in Table 2: (a) light optical micrograph of full nodule; (b) secondary electron micrograph of outer scale–inner scale interface with possible porosity/pullout; (c) secondary electron micrograph of the mixed oxide inner scale; (d) secondary electron micrograph of the internal oxidation layer.

ternal oxidation of the alloy, Fig. 3(d). While the precipitates were too fine to analyze using microprobe techniques, a scan of the area revealed that the composition resided in the two-phase region of Al_2O_3 and α-iron (substrate). The alloy did not contain significant amounts of oxygen once past the internal precipitate region.

4. DISCUSSION

4.1. Use of Fe–Al–S ternary phase diagrams

Development of the multiphase corrosion scale produced in the reducing gas can be understood by plotting the EPMA data on the ternary phase diagram (Fig. 4), in combination with the conventions summarized by Clarke [25] for plotting diffusion paths in multiphase ternary diffusion studies. By presenting the experimental data in this manner, the phase sequence and morphological development of the scale can be related to the composition path on the diagram. While this path should be plotted on the isothermal section corresponding to the exposure temperature, the only ternary phase diagram available was found at 900°C. Raghavan [32] has suggested that the diagram would deviate only

Table 2. EPMA data, in wt%, obtained for the corrosion scale formed in the oxidizing environment on the Fe–Al alloy. Features correspond to Fig. 3

Scale feature	Fe	Al	O	Phase(s)
Outer light gray phase	69.9 ± 0.2	0.0	30.4 ± 0.3	Fe_2O_3
Outer dark gray phase	72.3 ± 0.2	0.0	27.7 ± 0.1	Fe_3O_4
Inner dark gray phase	66.4 ± 0.2	4.0 ± 0.1	29.2 ± 0.5	$Fe_2O_3 + Fe_3O_4 + Al_2O_3$
Inner precipitate region	91.2 ± 0.7	5.5 ± 0.2	5.0 ± 0.2	α-(Fe) + Al_2O_3
Substrate near ppt region	95.3 ± 0.5	4.9 ± 0.4	0.2 ± 0.0	α-(Fe)
Alloy at far distances	95.1 ± 0.5	4.8 ± 0.6	0.2 ± 0.1	α-(Fe)

slightly at lower temperature isotherms, so it was considered for this analysis.

Figure 5 shows various portions of the diagram to aid in schematically tracing the path from the outer iron sulfide scale into the underlying alloy. One end of the "diffusion couple" may be considered to start at the gas–scale interface with the formation of a surface scale of iron sulfide, as found in Fig. 1(a), due to the outward diffusion of iron. Since no aluminum was found in the phase near the gas–scale interface, a point located on the Fe–S tie line at the iron sulfide composition can be found plotted on the ternary diagram, **a** in Fig. 5(b). As time increased, iron continuously diffused outward, thus thickening this outer scale. At the inner scale–outer scale interface, up to 1 wt% Al was found dissolved in the iron sulfide phase. This compositional variation measured in the iron sulfide phase is depicted by a solid line crossing the single phase region of iron sulfide with aluminum in solution, terminating at the two-phase field of $Fe_{1-x}S + \tau$ [**b** in Fig. 5(b)].

A linear interface was observed between the outer iron sulfide scale and the τ-phase at the intersection of these products. According to Clark [25], this is depicted by a dashed line, parallel to tie lines, crossing the two-phase field of $Fe_{1-x}S + \tau$ and terminating at the single phase region of τ, Fig. 5(c). The exact interfacial compositions of the phases are determined by the placement of the ends of the tie line, **b** in Fig. 5(b) and **c** in Fig. 5(c). In order to describe the inner scale, Figs 1(b) and (c), consisting of τ plates and iron sulfide particles, the layer may be considered as a single phase matrix of τ with precipitates of iron sulfide. For this morphology to occur, a solid line [line **c**–**d** in Fig. 5(d)] must dip into the single phase region of τ and return to the two-phase region of $\tau + Fe_{1-x}S$, indicating the visible thickness of the τ-phase at the interface. The diffusion path re-enters the two-phase region of $Fe_{1-x}S + \tau$ and then returns to the τ single phase region [line **d**–**e**–**f** in Fig. 5(d)], representing the isolated iron sulfide precipitates in the inner scale, Fig. 1(c). It is assumed that the path continues through the single phase τ region, through **g**, and terminates at the two-phase region of $\tau + (\alpha)$-Fe (**h**). A path of this type to describe the inner scale would incorporate the EPMA data obtained for the scan of the inner scale, represented by **e**, and for the τ plates, as indicated by **g**.

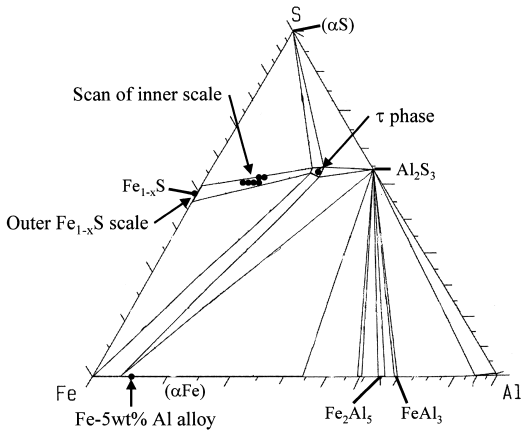

Fig. 4. Fe–Al–S ternary phase diagram at 900°C with overlaid EPMA data for the corrosion products and underlying substrate [32]. Axes are in weight percentages.

For the alloy–scale interface, a solid line crossing the two-phase region of $\tau + (\alpha)$-Fe, so as to cut tie lines in Fig. 5(e), can represent the locally equilibrated columnar two-phase region observed at the scale–alloy interface. As observed on the bottom of Fig. 1(b), this describes the nonplanar interfacial development of the τ plates with the alloy. This type of attack into the substrates helps to show why the two-phase inner scale is in the form of τ plates and iron sulfide particles. Penetration of the substrate in this manner would also indicate the inward diffusion of sulfur, most likely along phase boundaries ($Fe_{1-x}S$ and τ) or through the porosity, to form new product at the alloy–scale interface. Again, the interfacial compositions of τ and the alloy would be denoted by the ends of the tie line, **h** and **i** in Fig. 5(e). However, according to the diagram, the maximum amount of aluminum in the alloy is approximately 4 wt%. Therefore, it is possible that an aluminum depletion layer may exist in the alloy but is not detected by the electron microprobe (1 μm reaction volume).

An additional point to be made concerns the amount of aluminum found in solution in the iron sulfide near the inner scale–outer scale interface, point **2**. According to the ternary phase diagram supplied by Patnaik and Smeltzer [34], they quote 1.0 at.% Al (~0.6 wt%) as a maximum at 900°C. In this study, relatively high values of approximately 1 wt% Al (~2.0 at.%) was found at the lower temperature of 700°C. In addition, Strafford and Manifold have also observed 1 wt% Al in solution for similar temperature regimes during exposure to purely sulfidizing gases [6], and have found up to 4 wt% in solution for growth of FeS scales on Fe–Al alloys at 1000°C [7]. A possible explanation for these discrepancies may reside in the fact that the construction of the Fe–Al–S ternary phase diagram by Patnaik and Smeltzer [34] was conducted using Fe–Al alloys and bulk crystals of the sulfide phases. This may suggest that a thermally grown iron sulfide phase can dissolve more aluminum in solution than can a synthesized, bulk phase.

4.2. Use of Fe–Al–O ternary phase diagrams

Similar to the substrate attack in the reducing atmosphere, degradation of the Fe–Al substrate in

the oxidizing gas can also be analyzed by plotting the EPMA data on the ternary phase diagram containing oxygen, Fig. 6. However, due to the difference in corroding species (oxygen vs sulfur), the reaction products formed are now oxide phases.

Figure 7 shows various portions of the diagram to aid in schematically tracing the path from the outer Fe_2O_3 scale into the underlying alloy. The "diffusion couple" may again be considered to start at the gas–scale interface with the formation of the outer scales of Fe_2O_3 and Fe_3O_4, Fig. 3(a), due to outward diffusion of iron. These phases were represented by **a** and **b**, respectively, on Fig. 7(b). The linear interface that exists between the two iron oxide phases suggests parallel movement along the tie line between them. Again with time, these phases continue to thicken as iron diffuses outward. The next phase encountered was the darker gray oxide that grew inward into the Fe–Al substrate, Fig. 3(c). Development of this product was due to the penetration of oxygen into the alloy. The composition for this phase placed it near the corner of the three-phase region of Fe_2O_3–Fe_3O_4–Al_2O_3 [**c** on Fig. 7(b)]. The linear interface between these two phases again suggests movement parallel to tie lines, as seen by the arrow in Fig. 7(b) between **b** and **c**.

According to microprobe data, the next composition lies within the two-phase region of α-(Fe) + Al_2O_3, denoted by **d** in Fig. 7(c). These data

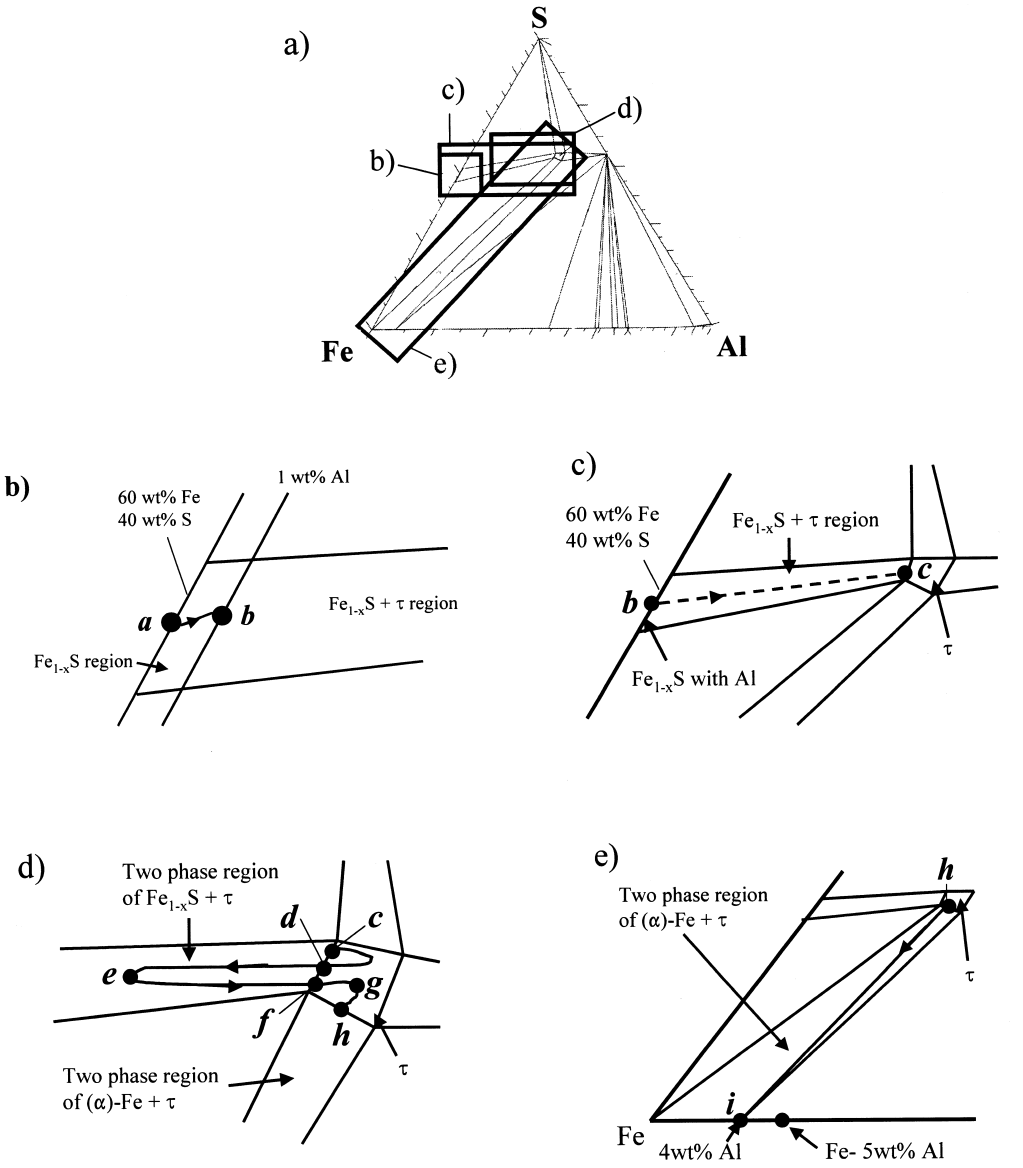

Fig. 5. Schematically drawn portions of the Fe–Al–S ternary phase diagram indicating the change in composition and plotting of a possible diffusion path.

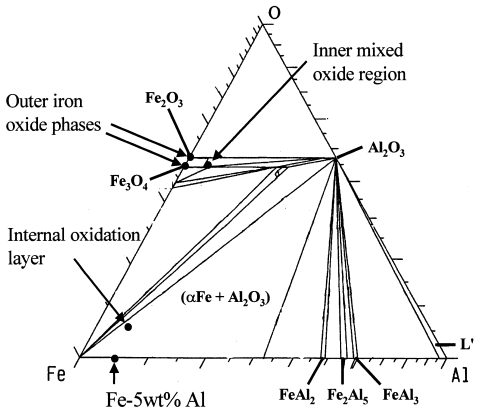

Fig. 6. Fe–Al–O ternary phase diagram at 700°C with overlaid EPMA data for the corrosion products and underlying substrate [33]. Axes in weight percentages.

were taken from the inner precipitate region observed in Fig. 3(d). However, in reviewing the Fe–Al–O diagram, it is impossible to traverse from the corner of the three-phase field, **c**, directly into the two-phase region, **d**. Therefore, another phase must exist between these two regions. Considering the literature, as well as the phase diagram, the most probable phase to form would be an alumina layer between the mixed oxide region and the internal precipitate layer. To support this possibility, investigations by Tomaszewski and Wallwork [5] have shown that a thin layer of alumina may form between the iron oxide phases and the alloy. With this assumption, the path appears to continue parallel to tie lines towards the alumina phase [arrow from **c** towards **e** in Fig. 7(b)]. Due to the appearance of a linear interface between the mixed oxide region (with possible thin alumina scale formation) and the internal precipitate region, the path again travels parallel to the tie lines through the two-phase region of α-(Fe) + Al_2O_3, line **e**–**f** in Fig. 7(c). From this path, it appears that localized regions of the matrix would be aluminum depleted due to the interfacial compositions being dictated by the ends of the tie line, as the alumina phase is richer in aluminum than the initial base material. In the two-phase region, the isolated precipitates observed in Fig. 3(d), which are most likely alumina formed due to the inward diffusion of oxygen, are depicted by a solid line dipping into the two-phase field of α-(Fe) + Al_2O_3 and terminating at the alloy composition of Fe–7.5Al (line **f**–**d**–**g**). Again, this type of path would encompass the EPMA data obtained from the scan of the individual layers, as well as the observed phase sequence.

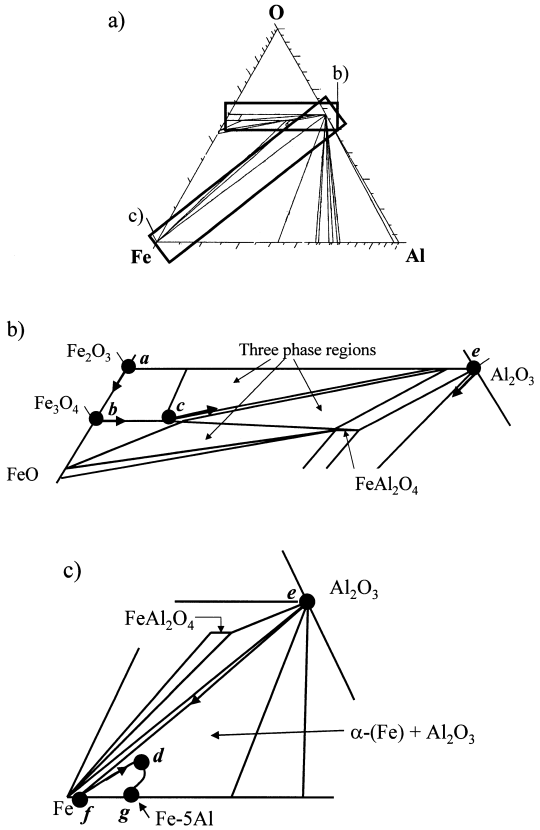

Fig. 7. Schematically drawn portions of the Fe–Al–O ternary phase diagram indicating the change in composition and plotting of a possible diffusion path.

5. SUMMARY

Conventional analysis of corrosion products formed on alloys due to high temperature gaseous exposure generally rely upon a number of microscopy and surface characterization techniques. These latter methods typically provide the quantitative chemical information and crystal structures necessary to gain an understanding of the corrosion reactions taking place. This paper has shown that through the integrated use of microscopy, electron probe microanalysis, and ternary phase diagrams, another viable approach to facilitate in the understanding of not only the corrosion reactions occurring, but also the corresponding phase layer sequence and resulting morphologies that the products attain, can be utilized as well.

Acknowledgements—This research was sponsored by the Fossil Energy Advanced Research and Technology Development (AR&TD) Materials Program, US Department of Energy, under contract DE-AC05-96OR22464 with Lockheed Martin Energy Research Corporation. The authors wish to thank V. K. Sikka and P. F. Tortorelli from ORNL for the cast Fe–Al alloys used in corrosion testing and technical discussions, respectively.

REFERENCES

1. Hagel, W. C., *Corrosion*, 1965, **21**, 316.
2. Saegusa, F. and Lee, L., *Corrosion*, 1966, **22**, 168.
3. Boggs, W. E., *J. electrochem. Soc*, 1971, **118**(6), 906.

4. Tomaszewski, P. and Wallwork, G. R., in *High Temperature Corrosion*, ed. R. A. Rapp. National Association of Corrosion Engineers, Houston, TX, 1981, pp. 258–266.
5. Tomaszewicz, P. and Wallwork, G. R., *Oxid. Metals*, 1983, **19**(5/6), 165.
6. Strafford, K. N. and Manifold, R., *Oxid. Metals*, 1969, **1**(2), 221.
7. Strafford, K. N. and Manifold, R., *Oxid. Metals*, 1972, **5**(2), 85.
8. Patnaik, P. C. and Smeltzer, W. W., *Oxid. Metals*, 1985, **23**(1/2), 53.
9. Patnaik, P. C. and Smeltzer, W. W., *J. electrochem. Soc*., 1985, **132**, 1226.
10. Smith, P. J., Jackson, P. R. S. and Smeltzer, W. W., *J. electrochem. Soc*., 1987, **134**(6), 1424.
11. Smith, P. J. and Smeltzer, W. W., *Oxid. Metals*, 1987, **28**, 291.
12. DeVan, J. H., in *Oxidation of High-Temperature Materials*, ed. T. Grobstein and J. Doychak. TMS, Warrendale, PA, 1988, pp. 107–115.
13. McKamey, C. G., DeVan, J. H., Tortorelli, P. F. and Sikka, V. K., *J. Mater. Res*., 1991, **6**(8), 1779.
14. DeVan, J. H. and Tortorelli, P. F., *Corros. Sci*., 1993, **35**(5–8), 1065.
15. Tortorelli, P. F. and DeVan, J. H., *Mater. Sci. Engng*, 1992, **A135**(1/2), 573.
16. DeVan, J. H. and Tortorelli, P. F., *Mater. High Temp*., 1993, **11**(1–4), 30.
17. Natesan, K., in *High Temperature Corrosion*, ed. R. A. Rapp. National Association of Corrosion Engineers, Houston, TX, 1991, pp. 336–344.
18. Tortorelli, P. F., Wright, I. G., Goodwin, G. M. and Howell, M., *Elevated Temperature Coatings: Science and Technology II*, Anaheim, CA, 4–8 February. TMS, Warrendale, PA, 1996, pp. 175–186.
19. Kai, W. and Huang, R. T., *Oxid. Metals*, 1997, **48**(1/2), 59.
20. Kai, W., Chu, J. P., Huang, R. T. and Lee, P. Y., *Mater. Sci. Engng*, 1997, **A239–240**, 859.
21. Banovic, S. W., DuPont, J. N. and Marder, A. R., *Weld. J*., 1999, **78**, 23s.
22. Prescott, R. and Graham, M. J., *Oxid. Metals*, 1992, **38**(3/4), 233.
23. Mrowec, S., *Oxid. Metals*, 1995, **44**(1/2), 177.
24. Smith, B. J., Goldstein, J. I. and Marder, A. R., *Metall. Mater. Trans. A*, 1995, **26A**, 41.
25. Clark, J. B., *Trans. Am. Inst. Min. Engrs*, 1963, **227**, 1250.
26. HSC Chemistry for Window, Version 3.0. Outokumpu Research Oy, Finland, 1997, www.outokumpu.fi/hsc.
27. Banovic, S. W., DuPont, J. N. and Marder, A. R., *Mater. Characterization*, submitted.
28. Goldstein, J. I., Newbury, D. E., Echlin, P., Joy, D. C., Romig Jr, A. D., Lyman, C. E., Fiori, C. and Lifshin, E., *Scanning Electron Microscopy and X-ray Microanalysis*, 2nd edn. Plenum Press, New York, 1992.
29. Mrowec, S., Walec, T. and Werber, T., *Oxid. Metals*, 1969, **1**(1), 93.
30. Mrowec, S. and Wedrychowska, M., *Oxid. Metals*, 1979, **13**(6), 481.
31. Banovic, S. W., DuPont, J. N. and Marder, A. R., *Oxid. Metals*, accepted.
32. Raghavan, V., in *Phase Diagrams of Ternary Alloys, Pt 2*. The Indian Institute of Metals, Calcutta, India, 1988, pp. 5–9.
33. Raghavan, V., in *Phase Diagrams of Ternary Alloys, Pt 5*. The Indian Institute of Metals, Calcutta, India, 1988, pp. 5–8.
34. Patnaik, P. C. and Smeltzer, W. W., *J. electrochem. Soc*., 1984, **131**, 2688.